GEOLOGICAL SURVEY OF CANADA
OPEN FILE 7853

Targeted Geoscience Initiative 4: Contributions to the Understanding of Volcanogenic Massive Sulphide Deposit Genesis and Exploration Methods Development

Integration of rock properties and geophysics, Bathurst Mining Camp

Peter A. Tschirhart[1,2] **and William A. Morris**[1]

[1]McMaster University, Hamilton, Ontario
[2]Sander Geophysics Ltd., Ottawa, Ontario

2015

This publication is available for free download through GEOSCAN (http://geoscan.nrcan.gc.ca/)

Recommended citation

Tschirhart, P.A. and Morris, W.A., 2015. Integration of rock properties and geophysics, Bathurst Mining Camp, *In:* Targeted Geoscience Initiative 4: Contributions to the Understanding of Volcanogenic Massive Sulphide Deposit Genesis and Exploration Methods Development, (ed.) J.M. Peter and P. Mercier-Langevin; Geological Survey of Canada, Open File 7853, p. 101–115.

Publications in this series have not been edited; they are released as submitted by the author.

Contribution to the Geological Survey of Canada's Targeted Geoscience Initiative 4 (TGI-4) Program (2010–2015)

TABLE OF CONTENTS

Integration of rock properties and geophysics, Bathurst Mining Camp

Peter A. Tschirhart[1,2]* and William A. Morris[1]

[1]School of Geography & Earth Sciences, McMaster University, 1280 Main Street West, Hamilton, Ontario L8S 4K1
[2]Present Address: Sander Geophysics Ltd., 260 Hunt Club Road, Ottawa, Ontario K1V 1C1
*Corresponding author's e-mail: ptschirhart@sgl.com

ABSTRACT

Physical rock property information is an important aspect of geophysical processing and interpretation as it provides a direct link between geophysical data and geological interpretations. Herein, the existing physical rock property (density and magnetic susceptibility measurements) database for host rocks and volcanogenic massive sulphide (VMS) mineralization in the Bathurst Mining Camp (BMC), northern New Brunswick, is expanded by incorporating new measurements taken on *in situ* samples and drill cores from throughout the BMC. Descriptive statistics are calculated and presented, and density-magnetic susceptibility bivariate plots are used to illustrate patterns indicative of changes in the abundances of paramagnetic versus ferrimagnetic mineral phases. A discrete object magnetic inversion, solving for the remanent magnetization vector of the Armstrong B anomaly, is computed. The inversion is constrained geometrically by geological mapping at surface and diamond drilling at depth. Magnetic susceptibility values for the country rock and mineralization are from the physical property database. Results of the inversion suggest that the remanent vector was acquired sometime between 470 and 420 Ma, likely during the Salinic orogeny. Density information is used to reprocess ground gravity and airborne gravity gradiometry (AGG) data by applying a laterally variable Bouguer and terrain density correction linked to averaged, measured density values and mapped extents of the different tectonostratigraphic groups that make up the BMC. The results of this reprocessing subtly change the gravity and gravity-gradient anomaly patterns allowing for isolated anomalies to be more discretely resolved and reduce the impact of the terrain-related signal in the AGG data. Finally, helicopter-borne frequency domain electromagnetic data for a small test site within the BMC are inverted for magnetic susceptibility and forward modelled into a magnetic anomaly grid. Magnetic susceptibility values from the physical property database are used to validate the results of the inversion. This computed near-surface magnetic anomaly grid is then used as a reference to effectively filter measured total magnetic intensity data to represent solely near-surface magnetic sources. Although petrophysical measurements in the BMC may not apply elsewhere, the various methodologies presented are appropriate wherever the geological and geophysical requirements of the method are met.

INTRODUCTION

Physical properties of rocks are controlled by their chemical and mineralogical composition, which in turn reflects the geological processes involved in the initial formation of the rock and any subsequent metamorphism, alteration, erosion, and weathering. Evaluation of systematic patterns of physical property variations is important in the synthesis of geological and geophysical data for mineral exploration. Lithological classifications are based on mineralogy and textures, with rock silica content being an import classification characteristic of many types of lithology. Geophysical data, however, typically reflect the spatial distribution of accessory minerals (e.g. presence of magnetic or conductive minerals) not commonly used as the defining criteria for geological classifications. A complete understanding of the relationship between the geological and geophysical physical properties allows for the extraction of additional information, creation of more accurate, constrained geophysical and geological models, refinements to data processing methodologies, and ground truths for new geophysical methods.

In the Bathurst Mining Camp (BMC), northeastern New Brunswick (Fig. 1), Mwenifumbo et al. (2003) performed multi-sensor downhole logging at the Stratmat, Halfmile Lake, and Restigouche deposits and compiled and presented these data. Thomas (2003) also presented density information for drill-core samples from the Brunswick 12, Canoe Landing Lake, Heath Steele, Key Anacon, and Willet deposits. The integration of disparate individual datasets, however, may not be straightforward. Commonly, tools used for borehole logging are not cross-calibrated with tools used for core logging. Apparent differences in physical property values can also arise from factors, such as variations in borehole diameter, changes in sensor frequency, and

Tschirhart, P.A. and Morris, W.A., 2015. Integration of rock properties and geophysics, Bathurst Mining Camp, *In:* Targeted Geoscience Initiative 4: Contributions to the Understanding of Volcanogenic Massive Sulphide Deposit Genesis and Exploration Methods Development, (ed.) J.M. Peter and P. Mercier-Langevin; Geological Survey of Canada, Open File 7853, p. 101–115.

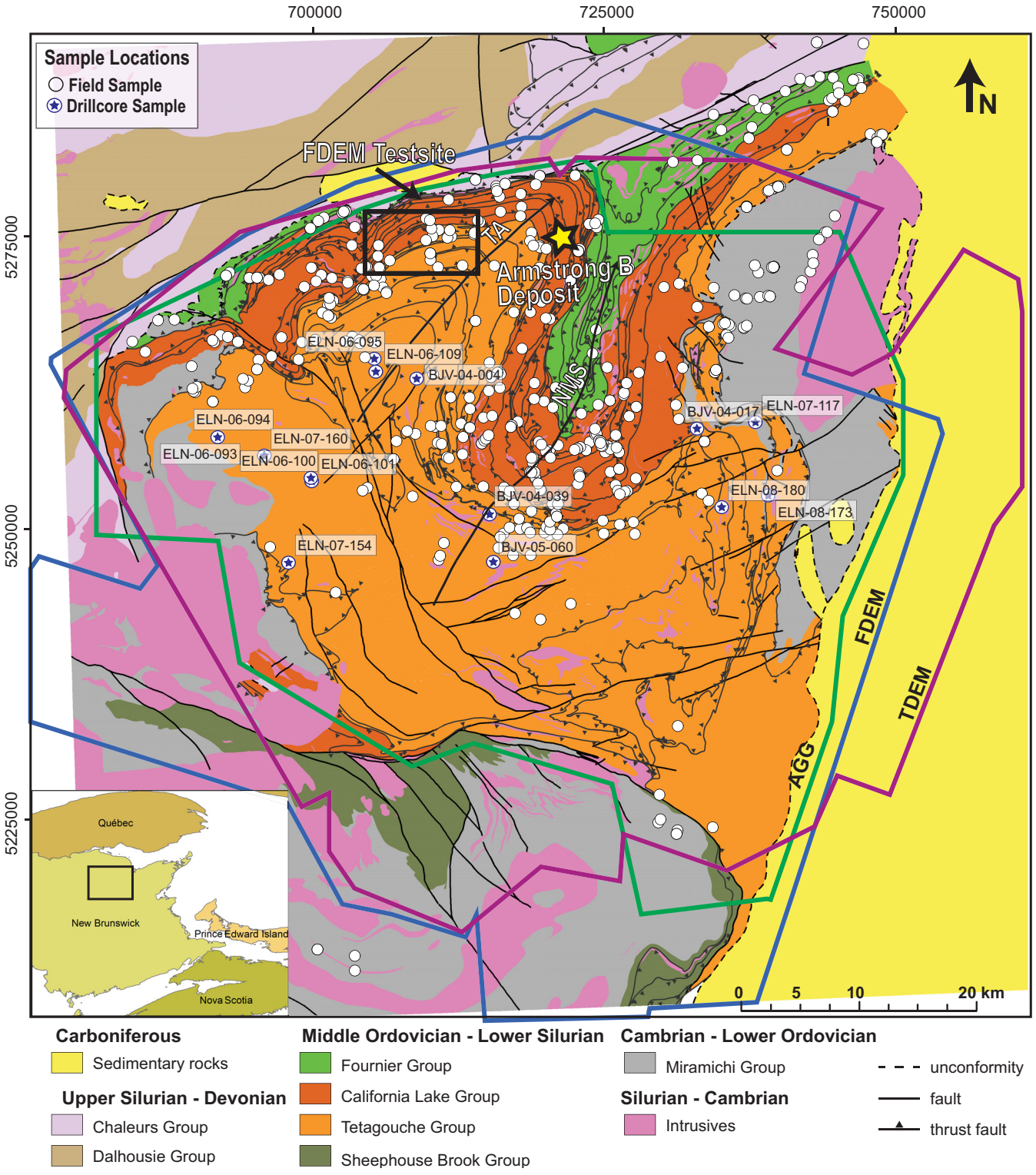

Figure 1. Tectonostratigraphic map of the Bathurst Mining Camp (modified from van Staal et al., 2003). Abbreviations: Airborne geophysical survey boundaries identified: AGG = Airborne gravity gradiometry survey; FDEM = frequency domain electromagnetic survey; NMS = Nine Mile Synform; TA = Tetagouche Antiform; TDEM = time domain electromagnetic survey. Rock property sample locations are shown as white circles.

measurement procedure. Borehole and core rock property datasets are best considered independently unless it can be shown that they are statistically equivalent. The initial objective of our study was to expand the physical property database presented in Thomas (2003) by incorporating new density and magnetic susceptibility information collected for drill-core samples and *in situ* field stations throughout the BMC. The density measurements were obtained using Archimedes' submersion approach and magnetic susceptibility were calculated by averaging three measurements taken on each sample. Descriptive statistics of the newly compiled density and magnetic susceptibility measurements are presented in tables and subjected to bivariate analyses to extract additional geological information.

The magnetic susceptibility data are then used as a constraint for a 3-D magnetic inversion model of the Armstrong B deposit to solve for the direction and intensity of the remanent vector associated with the magnetic anomaly of the deposit. The density data are used to develop a new Bouguer and terrain correction factor for ground gravity and airborne gravity gradiometry (AGG) by using a spatially variable density averaged from density measurements and linked to the geological map expression. Finally, a subset of the magnetic susceptibility measurements are used to ground-truth magnetic susceptibility values obtained from inversion of frequency domain airborne electromagnetic data (FDEM). The inverted magnetic susceptibility values are then used to forward model the total magnetic intensity and develop a new near-surface magnetic residual map for a small area northwest of the Tetagouche Antiform in the BMC (Fig. 1).

GEOLOGY

The BMC encompasses a semi-circular area of approximately 70 km in diameter in the Miramichi Highlands of northern New Brunswick (Fig. 1). Part of the larger Brunswick subduction complex (BSC), the BMC records the Late Ordovician – Silurian development, closure, and subduction of the Tetagouche-Exploits back-arc basin (van Staal et al., 2003). Felsic to mafic back-arc volcanogenic rocks with coeval sedimentary rocks of the California Lake, Tetagouche, Fournier, and Sheephouse Brook tectonic blocks diachronously developed in separate subbasins, sharing a common tectonic environment along the margin of the Laurentia continent (Rogers et al., 2003). The Tetagouche, Sheephouse Brook, and at least part of the California Lake blocks are underlain by rocks of the Miramichi Group that form the stratigraphic basement and are the oldest exposed sedimentary and volcanic rocks of the Bathurst Supergroup (van Staal et al., 2003). During the Late Ordovician – Late Silurian, these adjacent terranes were incorporated into the BSC during the Salinic orogeny (van Staal et al., 2008). Multiple phases of felsic through mafic intrusions were emplaced throughout the BMC during Ordovician, Silurian, and Devonian times. Sedimentary cover sequences, including the Silurian Chaleur and Kingsclear groups, Devonian Dalhousie Group, and Carboniferous Clifton Formation, occupy the edges of the BMC map region. A thorough discussion of the geology and tectonostratigraphy of each tectonic block is given in van Staal et al. (2003) and van Staal et al. (2008).

Deformation in the BMC was polyphase and long-lived, forming complex structures and tectonostratigraphic relationships. From the Ordovician through to the Early Silurian, ongoing subduction resulted in a series of tectonic blocks that were structurally juxtaposed and imbricated into a series of nappes. D_1 and D_2 thrusting created older over younger relationships both locally within individual nappes, and regionally across tectonic blocks (van Staal et al., 2003). Regional high-pressure, low-temperature penetrative deformation followed closure of the complex. D_3 and D_4 structures overprint D_1 and D_2 during unroofing and exhumation of the BMC.

D_1 thrust-related deformation is recognized as causing M_1 conditions (350–400°C, 5.5–5.8 kbar) across the BMC during the Ashgillian to Llandoverian (Currie et al., 2003). Assembly and steepening of the BMC nappes (with contained deposits) was likely complete by this time. Later metamorphism (M_2) has been recognized elsewhere in the BSC but its effect on the rocks of the BMC is minimal or absent (van Staal, et al., 2008).

RESULTS

Statistical Analysis

Statistical analysis of the expanded rock property database is presented in Tschirhart and Morris (2014). Physical property measurements made on the drill-core rock samples were divided into subpopulations based on their lithological classification. Statistical parameters (mean ($\overline{x}$), standard deviation (s), 25th, 50th (median), and 75th quartiles (Q_1, Q_2, and Q_3, respectively) were calculated from the density and magnetic susceptibility measurements and are listed in Tables 1 and 2, respectively. Henkel (1994) published a graphical template based on a comparison of magnetic susceptibility and density data that permits the discrimination between paramagnetic minerals (principally weakly magnetic biotite, amphibole, and pyroxene) and ferrimagnetic minerals (strongly magnetic magnetite and pyrrhotite) (Fig. 2a). Using this template it is possible to identify data trends (reduced susceptibility and density) indicative of the change in physical rock properties that may arise from the progressive effects

Table 1. Density statistics. $\overline{x}$ = mean; s = standard deviation, Q_1, Q_2, and Q_3 = 25th, 50th, and 75th quartiles, respectively.

Rock Type (N=1271)	**Density** (g/cm³)					
	N	$\overline{x}$	s	Q_1	Q_2	Q_3
Mafic *(N=165)*						
Basalt	105	2.85	0.11	2.77	2.86	2.93
Blueschist	9	2.88	0.08	2.84	2.86	2.92
Diabase	7	2.91	0.08	2.86	2.88	2.94
Gabbro	36	2.90	0.11	2.82	2.87	2.99
Mafic dyke	8	2.91	0.07	2.93	2.93	2.94
Sedimentary *(N=240)*						
Argillite	37	2.79	0.04	2.76	2.78	2.82
Graphitic argillite	11	2.76	0.04	2.73	2.75	2.78
Chert	8	2.68	0.08	2.65	2.69	2.72
Phyilite	8	2.78	0.10	2.72	2.76	2.84
Phylonite	2	2.73	0.06	2.71	2.73	2.75
Quartzite	11	2.68	0.05	2.64	2.68	2.71
Sericite-chlorite-altered sedimentary rocks	12	2.81	0.04	2.79	2.80	2.83
Shale	30	2.72	0.10	2.66	2.72	2.77
Siltstone	16	2.65	0.09	2.63	2.68	2.69
Siltstone and shale*	107	2.74	0.09	2.68	2.74	2.79
Slate	8	2.73	0.09	2.67	2.70	2.75
Tuffaceous sedimentary rocks	21	2.83	0.08	2.77	2.81	2.87
Turbidite	5	2.73	0.15	2.64	2.67	2.76
Iron Formation *(N=10)*						
Iron formation	10	3.00	0.15	2.93	2.97	3.02
Felsic-Intermediate *(N=806)*						
Granite	5	2.62	0.07	2.57	2.58	2.68
Ash tuff	30	2.71	0.05	2.68	2.71	2.73
Crystal tuff	193	2.73	0.05	2.70	2.73	2.75
Dacite	4	2.68	0.01	2.66	2.68	2.69
Felsic tuff	82	2.74	0.07	2.70	2.74	2.78
Quartz feldspar augen schist	11	2.69	0.08	2.67	2.68	2.76
Quartz feldspar porphyry	163	2.69	0.07	2.65	2.70	2.72
Rhyolite	225	2.71	0.07	2.67	2.71	2.74
Rhyolite agglomerate	22	2.69	0.03	2.66	2.68	2.71
Rhyolite tuff	45	2.72	0.10	2.64	2.72	2.75
Volcaniclastic	30	2.70	0.10	2.64	2.70	2.74
Sulphide *(N=50)*						
Massive	17	3.74	0.94	3.20	3.73	4.21
Semi-massive	13	3.04	0.21	2.90	3.08	3.10
Disseminated	20	2.94	0.89	2.88	2.93	3.00

*Uses 30 shale and 16 siltstone samples listed plus 61 additional samples that were not classified as either lithology

of hydrothermal alteration. To apply this approach to the many lithological units present in the BMC, the measurements were divided into a small number of rock classification subdivisions (felsic, mafic, sedimentary, iron formation, and sulphide), which are more appropriate for regional-scale investigations.

Perhaps the most important conclusion from this exercise is that none of the various lithological types can be fully represented by a tight (restricted) density or susceptibility range. Rather, the Henkel plots show that each rock type exhibits some variation in density and susceptibility values (Fig. 2a,b,c). These physical property variations are likely related to the effects of localized alteration or regional-scale metamorphic effects. However, without comparing results from several adjacent boreholes, it is not possible to outline any such patterns. Hydrothermal alteration influences the physical properties in two ways. The most common effect detected in sedimentary, tuffaceous, and some of the mafic volcanic rock samples is progressively increasing density values with a moderate increase in magnetic susceptibility. The hydrothermal alteration process imparts a progressive change in the abundance of paramagnetic minerals accompanied by an increase in density, perhaps as a result of porosity reduction during alteration. The second effect, best exhibited by the sedimentary rocks, is a much larger change in the magnetic susceptibility accompanied by a smaller change in density (Fig. 2b). The prevailing hypothesis is that during hydrothermal alteration, ferrimagnetic minerals within the host rock are altered to weakly magnetic paramagnetic minerals (Mwenifumbo et al., 2003). This hypothesis partly implies that density is systematically affected (reduced) by the alteration process, as the data show. Henkel's (1994) template defines separate trends for ferromagnetic- and paramagnetic-bearing rocks. Although most of the measurements of mafic volcanic samples plot in the paramagnetic mineral grouping, there are also a lesser number of samples that form a distinct cluster in the ferrimagnetic mineral grouping. In particular it should be noted that measurements of basalt samples (Fig. 2c) plot in both groups, suggesting that geophysical modelling must consider both weakly and strongly magnetic basalt. Sulphide samples were subdivided into three classes: massive (>75 vol% sulphides), semi-massive (25–75 vol% sulphides), and disseminated (sulphide grains not interconnected, typically with 25–75 vol% sulphides). The massive sulphide samples all plot in a region of high density and ferrimagnetic susceptibility (Fig. 2d), as expected. However, the density of the massive samples is quite variable. Gravity surveys are most effective in directly detecting sulphide bodies that are massive and of uniformly high density in a low-density country rock. Samples of disseminated and semi-massive sulphides plot in a well defined trend of increasing susceptibility with moderate increase in density (Fig. 2d). This trend reflects high contents of pyrrhotite and magnetite. The massive sulphide samples all plot within the region where ferrimagnetism predominates, except for one outlier with an anomalously low susceptibility. This relationship suggests that volcanogenic massive sulphide (VMS) mineralization may be associated with aeromagnetic anomalies that are controlled by remanent magnetism.

Table 2. Magnetic susceptibility statistics. $\bar{x}$ = mean; s = standard deviation, Q_1, Q_2, and Q_3 = 25th, 50th, and 75th quartiles, respectively.

		Susceptibility (SI)				
	N	$\bar{x}$	s	Q_1	Q_2	Q_3
Rock Type (1271)		*(SI x 10-3)*	*(SI x 10-6)*	*(SI x 10-3)*	*(SI x 10-3)*	*(SI x 10-3)*
Mafic *(N=165)*						
Basalt	105	0.48	4.90	0.24	0.36	0.54
Blueschist	9	2.66	6.60	0.42	2.13	10.35
Diabase	7	0.47	6.00	0.22	0.30	0.38
Gabbro	36	0.37	3.10	0.24	0.38	0.48
Mafic dyke	8	0.81	5.50	0.30	0.54	0.85
Sedimentary *(N=240)*						
Argillite	37	0.25	2.34	0.15	0.24	0.34
Graphitic argillite	11	0.23	4.63	0.11	0.18	0.11
Chert	8	0.40	7.30	0.15	0.28	0.52
Phyilite	8	0.23	1.72	0.16	0.22	0.34
Phylonite	2	0.14	1.69	0.12	0.14	0.17
Quartzite	11	0.05	3.00	0.02	0.06	0.10
Sericite-chlorite-altered sediments	12	0.26	1.64	0.18	0.31	0.36
Shale	30	0.21	5.95	0.10	0.18	0.36
Siltstone	16	0.09	5.29	0.04	0.08	0.14
Siltstone and shale*	107	0.20	5.14	0.09	0.19	0.51
Slate	8	0.19	2.47	0.13	0.19	0.29
Tuffaceous sedimentary rocks	21	1.08	4.84	0.41	0.79	2.60
Turbidite	5	0.22	1.70	0.18	0.20	0.38
Iron Formation *(N=10)*						
Iron formation	10	4.59	4.73	1.17	3.53	17.81
Felsic-Intermediate *(N=806)*						
Granite	2	0.05	2.50	0.03	0.05	0.08
Ash tuff	30	0.11	2.10	0.06	0.10	0.18
Crystal tuff	193	0.09	2.80	0.05	0.11	0.18
Dacite	3	0.05	4.00	0.03	0.05	0.09
Felsic tuff	82	0.11	3.00	0.06	0.12	0.24
Quartz feldspar augen schist	11	0.11	2.30	0.05	0.16	0.20
Quartz feldspar porphyry	163	0.05	3.30	0.02	0.05	0.12
Rhyolite	225	0.08	3.60	0.05	0.09	0.18
Rhyolite agglomerate	22	0.04	3.30	0.01	0.04	0.09
Rhyolite tuff	45	0.08	4.00	0.03	0.08	0.18
Volcaniclastic	30	0.05	3.90	0.01	0.05	0.14
Sulphide *(N=50)*						
Massive	17	5.99	8.67	2.05	8.87	26.18
Semi-massive	13	1.02	9.84	0.13	0.49	7.02
Disseminated	20	1.48	7.78	0.44	0.67	8.10

*Uses 30 shale and 16 siltstone sample listed plus 61 additional samples that were not classified as either lithology.

Samples of iron formation, an important ore equivalent (time-stratigraphic) marker horizon and exploration vector in the BMC (Peter et al., 2003), plot in two distinct populations; a higher susceptibility, lower density population, and a lower susceptibility, higher density population (Fig. 2e). These two populations are believed to correspond to the two distinct types of iron formation that are encountered in the camp; a Llanvirn-hematite rich (type 1) and an Aregian-magnetite rich (type 2). The distinction is significant as type 2 iron formation is more commonly associated with sulphide mineralization (Goodfellow and McCutcheon, 2003).

Constrained 3-D Geophysical Modelling

The Armstrong B deposit is located on the east limb of the Tetagouche Antiform (TA) (Fig. 1). The deposit consists of disseminated to massive sulphides hosted in a mixed sequence of ash, feldspar-crystal, and lithic-lapilli tuff of the Spruce Lake Formation (SLF) (Thomas et al., 2000). Due to the presence of abundant magnetically susceptible pyrrhotite, the lens-shaped deposit generates a 50 nT anomaly with the surround-

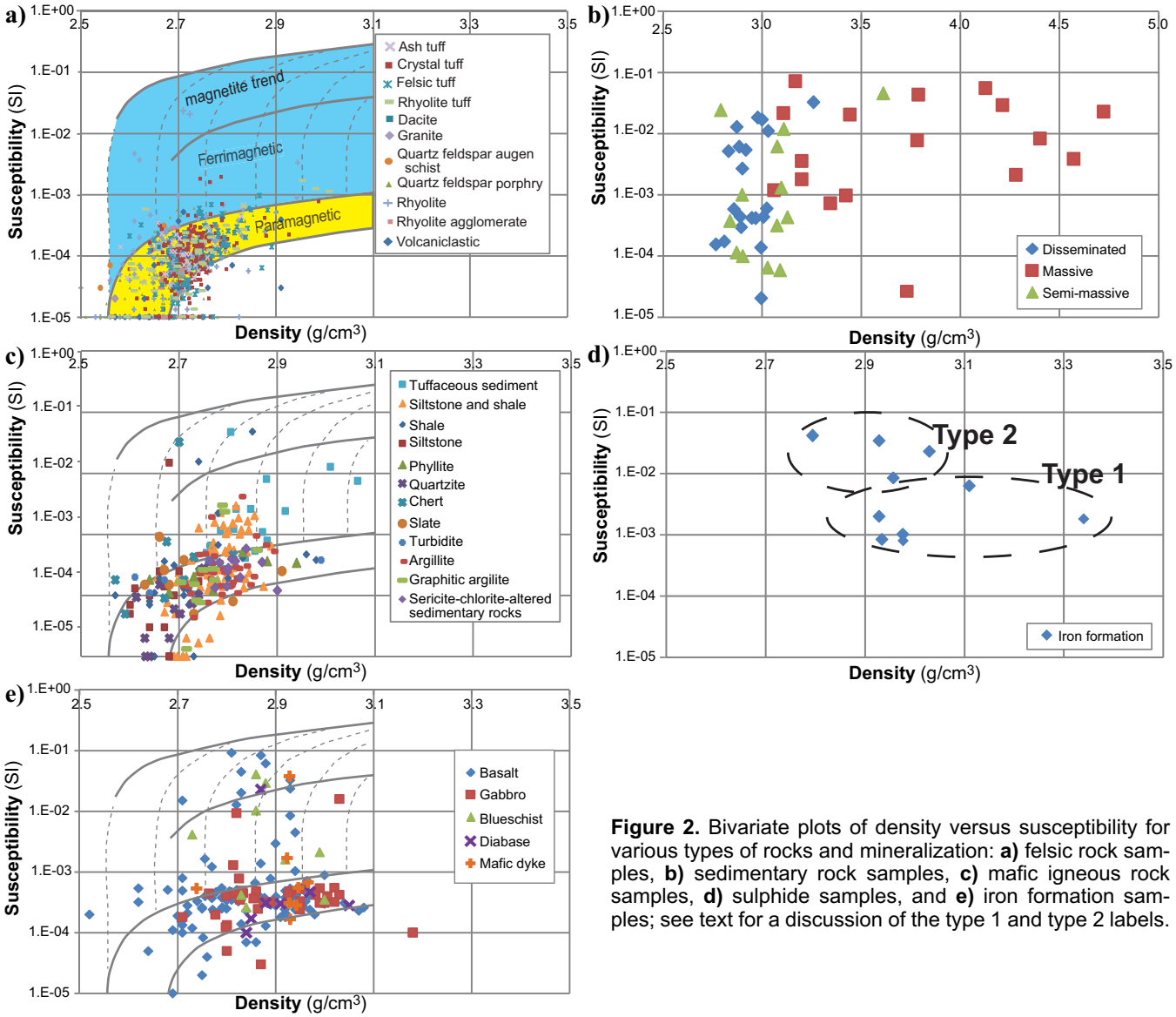

Figure 2. Bivariate plots of density versus susceptibility for various types of rocks and mineralization: **a)** felsic rock samples, **b)** sedimentary rock samples, **c)** mafic igneous rock samples, **d)** sulphide samples, and **e)** iron formation samples; see text for a discussion of the type 1 and type 2 labels.

ing magnetically weak felsic tuffs of the SLF (Fig. 3a). We applied a discrete object inversion approach using *pb*Encom Modelvision® software in which we fixed source body position, inducing field, strike length, and magnetization, and inverted for the residual total magnetization, body width, and body depth extent. The location and geometry of the deposit is well defined by several drillholes that intersect mineralization. This information, together with our petrophysical property measurements, was used to forward model the deposit as a steeply dipping (65°), northerly striking (15°) tabular body of 244 m length with an average magnetic susceptibility of 6 × 10^{-3} SI. The hosting SLF was assigned a magnetic susceptibility of 0.1 × 10^{-3} SI. The starting model is shown in Figure 3b.

The result of the inversion is shown in Figure 3c and 3d for the magnetic anomaly and geometric model, respectively. The root-mean-square error (RMSE) between the observed field (Fig. 3a) and the modelled field (Fig. 3c) is 2.8 nT (<1% of total signal) and closely matches the observed field. The misfit between the observed and calculated anomalies can be attributed mainly to an interfering magnetic anomaly associated with adjacent sources to the southwest and along the eastern edge of the study area. During the inversion computation, the estimated width of the magnetic source body increased from 25 to 165 m. This may be due to a resolution limitation imposed by the height of the magnetic sensor above the ground and the sampling rate of the sensor. Also, it is possible that the model is describing the orebody and its alteration halo, which may contain sufficient pyrrhotite to also register as a magnetic anomaly. The depth extent is also increased from 183 to 343 m, which can be attributed to the inaccurate depth extent determinations commonly inherent in geophysical inversion models (Spicer, 2010).

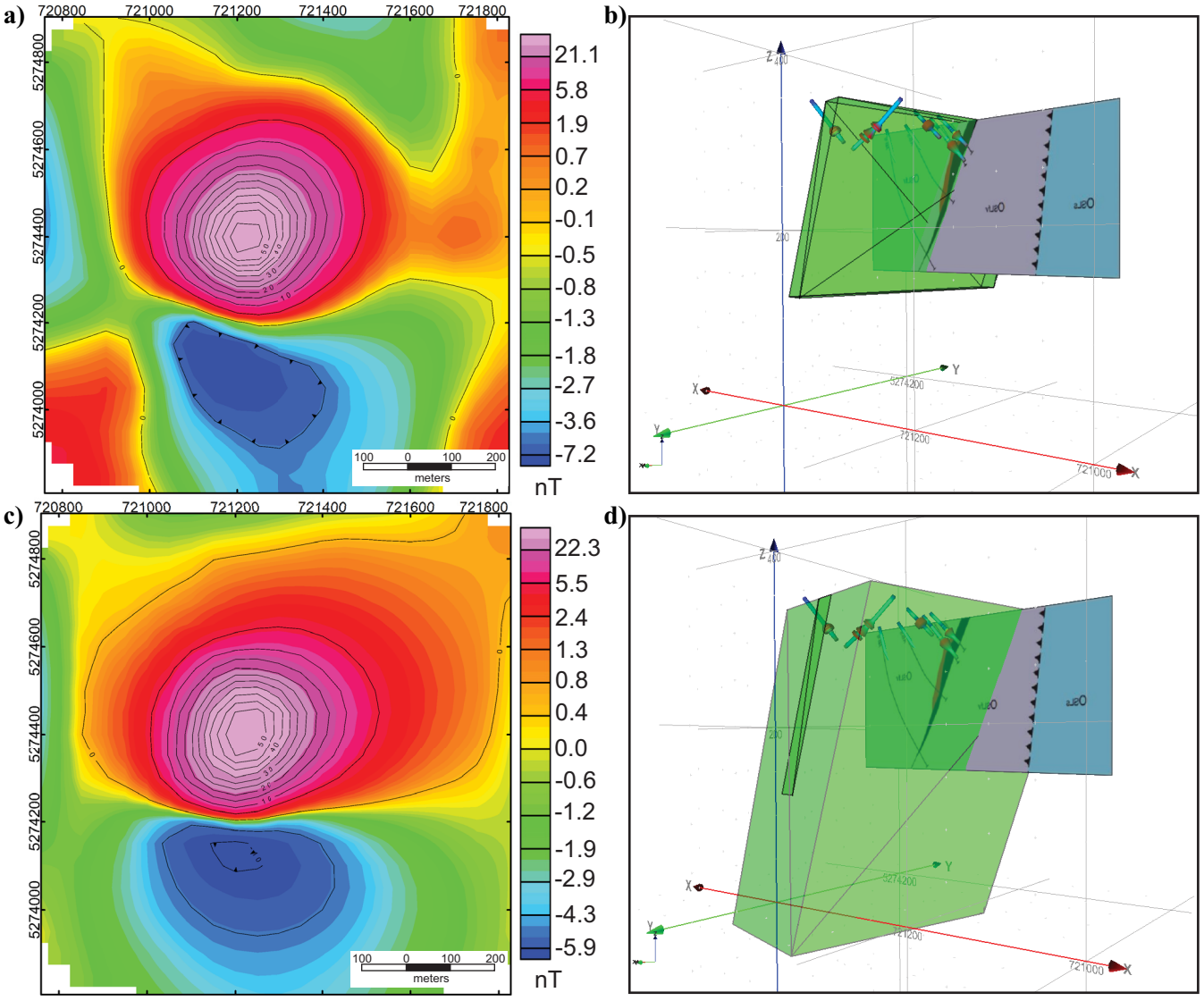

Figure 3. Starting model and solution of the Armstrong B deposit anomaly discrete object magnetic-inversion: **a)** observed magnetic anomaly; **b)** input 3-D discrete body geophysical model; **c)** calculated magnetic anomaly from inversion; and **d)** resultant discrete body model.

Acquisition or blocking of remanence is always linked to a geological event, whether it is primary deposition, later thermochemical recrystallization, or fluid flow associated with peak metamorphism or deformation. The upper age bound for remanence acquisition is the depositional age of the hosting SLF; 471 Ma (New Brunswick Dept. of Energy and Mines, 2013), whereas the lower age limit compatible with the geological evidence is the end of the Salinic orogenic episode ca. 418 Ma (van Staal et al., 2008). We speculate that the remanence most likely was imparted during D_1 or D_2 deformation when the sulphides were recrystallized (Goodfellow and McCutcheon, 2003). Using the Phanerozoic Apparent Polar Wander Path (APWP) published by Torsvik et al. (2012) for the Laurentian supercontinent, the expected remanence directions for the location of the Armstrong B deposit during the time period from 470 to 420 Ma can be estimated. The Koenigsberger (Q) ratio solved from the inversion is 1.4, implying that the remanent magnetization is of a higher magnitude than the inducing field. The remanent inclination and declination estimated by the inversion are I = -7° and D = 172°, respectively. Paleomagnetic results reported by Liss et al. (1993) from pillow basalts of the Tetagouche Group, sampled to the east of the Armstrong B deposit, give a mean *in situ* remanence direction of I = -6°, D = 140° that is not grossly dissimilar to the direction determined by modelling and inversion.

The remanence direction computed through the inversion differs from the APWP-derived remanence direction by slightly more than 30°. Most of this difference is attributed to the inclination of the computed remanence vector. This may be due to either (1) the

computed direction containing some portion of the present Earth's field that is the Koenigsberger ratio is higher than estimated or (2) the rocks have been tectonically rotated (tilted) subsequent to acquisition of the remanence direction. If (1) is valid, then the model remanence vector should fall on a great circle path between the present Earth's field direction and the expected remanence direction. Alternatively, if (2) is correct, then the difference between the model remanence direction and the expected remanence direction should fall on a small circle path with the axis of the small circle describing the strike of the fold axis. Based on the evidence provided by this study, it is not possible to definitively differentiate between the two options; however, (1) does outline a simple great circle path that intersects the apparent polar direction path within the time period 430 to 420 Ma. This time span coincides with the estimated peak of the Salinic orogeny: 430–423 Ma (van Staal et al., 2008). In contrast, (2) requires a tilt of approximately 30°, but the strike of this tilt rotation axis is perpendicular to the current strike of the Armstrong B deposit, and on this basis, (2) can be discounted. In summary, the Armstrong B deposit is has a strong remanent magnetization signal. Acquisition of this remanence occurred when the metamorphic temperatures cooled sufficiently to block the magnetization. The extant conclusion (1) also suggests that the orebody has been subject to only limited tectonic rotation since remanence acquisition.

Laterally Variable Density Correction

A detailed understanding of the physical rock properties is not only useful for petrophysical analysis and geophysical modelling, but also for improving the correction factors that are commonly applied to some geophysical data. Bouguer and terrain corrections in ground gravity calculations both require input of a density value that is reflective of the near-surface density. Airborne gravity gradiometer surveys measure the gravity gradient at some height above the topographic surface. As such, the primary signal recorded by an AGG survey is dominated by the density contrast between the topography and the air. To derive geologically meaningful information from these data it is necessary to apply a terrain correction, which requires a density estimate. Most commonly, a constant density of 2.67 g/cm^3 is used for these data corrections, as this value is considered to be the average density of crystalline, continental crust of granitic composition (Hinze, 2003). In many areas, including the BMC, universal application of this single correction value may introduce error into the reduced dataset. If the density of the near-surface rocks is higher (or lower) than the average density value, then elements of the topographic signal will be retained in the resulting data grid image. In areas where the geology comprises a series of lithologically distinct tectonic slices separated by thrust boundaries (such as in the BMC), it is possible (even likely) that the average surface density of each tectonic slice could be significantly different (Vajk, 1956). Tschirhart et al., (submitted) address this issue and propose application of a spatially variable density for Bouguer and terrain correction for ground gravity and terrain correction for airborne gravity gradiometry data. The correction factor used is determined using the mapped geology and measured density values. Briefly, a local average density that is reflective of a specific tectonostratigraphic group in the BMC is calculated from the measured physical property information. This local average density is then only applied to measurements taken within that area, as mapped by van Staal et al., (2003). With all measurements processed accordingly, the corrected data are combined and gridded.

Original ground gravity data reduced using a constant density of 2.67 g/cm^3 for the Bouguer and terrain correction are shown in Figure 4a. Ground gravity data reprocessed using a variable density for the Bouguer and terrain corrections are shown in Figure 4b. The difference between the constant and laterally variable density corrections is shown in Figure 4c. For the AGG data, the terrain correction was originally preformed using a variety of terrain correction densities ranging from 2.40 to 3.00 g/cm^3; for brevity only AGG G_{zz} (vertical gravity gradient) data corrected with a terrain density of 2.70 g/cm^3 are presented in Figure 4d. The G_{zz} component of the reprocessed AGG data using the laterally variable density correction are presented in Figure 4e, and the difference between the G_{zz} components of the constant (2.70 g/cm^3) and the laterally variable terrain correction is shown in Figure 4e. The differences in the final results using the constant correction and the spatially variable correction are subtle. For ground gravity, the overall shapes and trends of the major anomalies are unchanged by the reprocessing (Fig. 4c); however, the exact extents and amplitudes of these anomalies are altered. The major central gravity high, caused by the ophiolitic Fournier Group (Fig. 4a) and mafic volcanic rocks of the California Lake Group, is extended slightly to the east by tens of metres and is reduced in amplitude by a maximum of 2.1 mGal (Fig. 4c). Along the Tetagouche – California Lake contact, a small isolated body of dense Flat Landing Brook mafic volcanic rocks adjacent to the dense California Lake Group mafic volcanic rocks to the north is better resolved using the variable density method (Fig. 4c). By using a variable density method, a lower density correction value is applied to the Tetagouche Group than to the California Lake Group. A larger correction is applied to the groups containing higher density rock

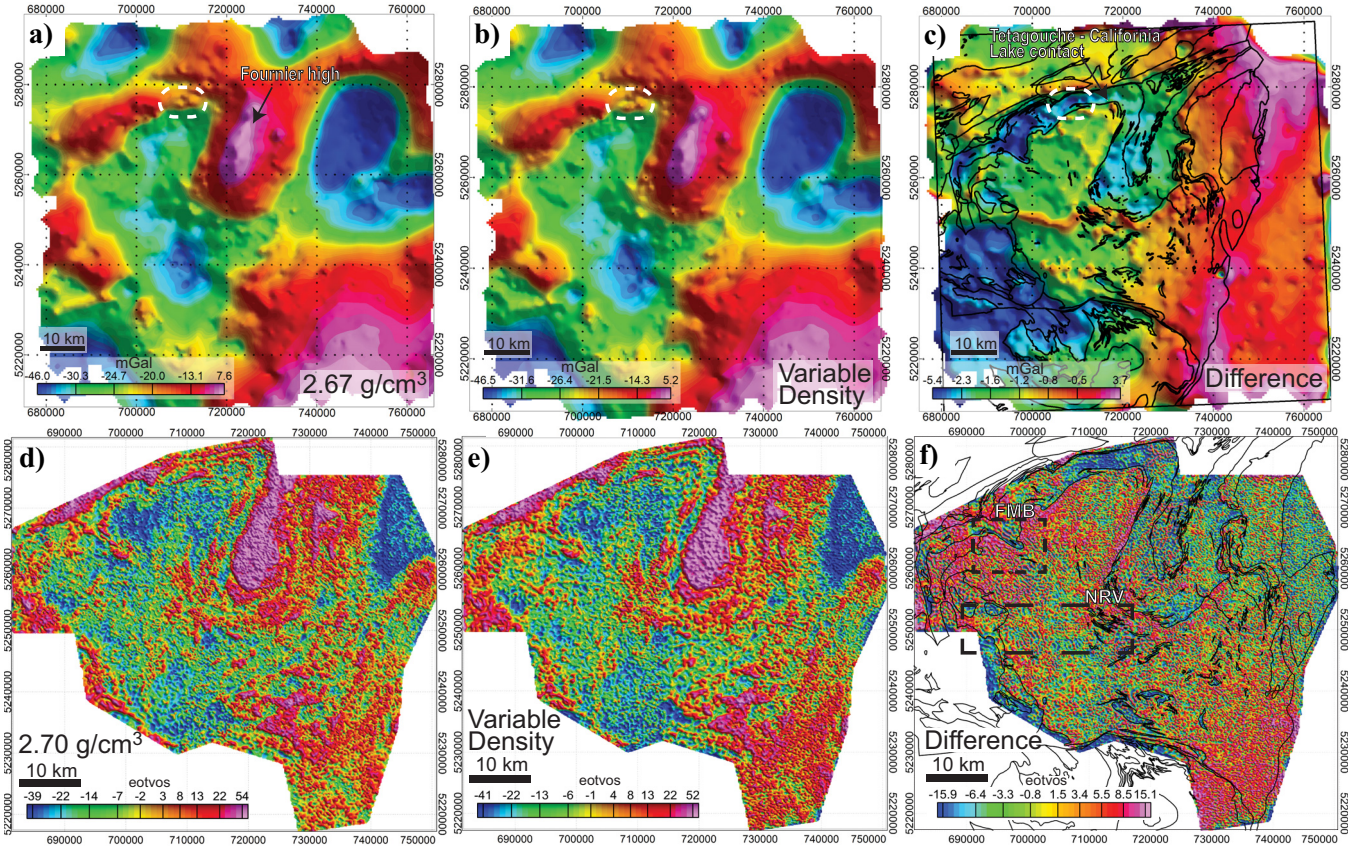

Figure 4. Constant density-corrected and laterally variable density-corrected gravity and gravity gradiometry (G_{zz}) maps and difference grids: **a)** ground gravity data map corrected using 2.67 g/cm^3; **b)** laterally variable density-corrected ground gravity map; **c)** difference between constant and laterally variable density-corrected ground gravity maps; **d)** Gzz component map corrected using 2.70 g/cm^3; **e)** laterally variable density-corrected G_{zz} component map; and **f)** difference between constant and laterally variable density corrected G_{zz} components. Circled area in (a) and (c) is discussed in the text. Abbreviations: FMB = Forty Mile Brook drainage basin; NRV = Nepisiguit River Valley.

units, and a smaller correction to those groups containing less dense rocks; thus, anomalously dense bodies within the less dense group become more pronounced/evident near more dense groups.

For AGG data, the difference between the constant density (Fig. 4d) and laterally variable density terrain corrected grid (Fig. 4e) is also subtle (Fig. 4f). The differences become much more apparent upon comparison of the end members of the constant terrain correction grids (i.e. 2.40 and 3.00 g/cm^3; Tschirhart et al., submitted). Locally, where the geological density matches the correction value, this incremental method may be appropriate. However, across larger areas, where near-surface density variations are complex due to structural and stratigraphic controls, this introduces considerable error. This applies for all tensor components, but for brevity is only shown for G_{zz} (Tschirhart, 2013). The influence of the Nepiguit River Valley (NRV), for example, appears to interfere with the true G_{zz} anomaly, producing false positives and negatives; however, this is minimized within the variable density grid by implying a correct reduction value (Fig. 4e).

Nettleton (1939) proposed that it is possible to determine the density of a topographic feature by iteratively searching for the minimum variance in a gravity signal profile after applying all appropriate terrain corrections. Exactly the same concept can be applied to gravity and topographic grids. Using two examples where there are marked differences in the gradient anomaly using different terrain correction values (NRV and part of the Forty Mile Brook (FMB) drainage basin) it is possible to determine the relationship of topography to the G_{zz} anomaly by plotting the covariance between G_{zz} and the topography against different density correction values (FitzGerald et al., 2011; Tschirhart et al., submitted). Covariance is a measure of the similarity between the morphology of the topographic and gravity image surfaces. The slope of the line of best fit between covariance and density reflects the importance of topography, with a steeper slope indicating greater importance. At the x-intercept, where covariance is zero, the G_{zz} anomaly should have no correlation with topography, and an optimum density correction value can be found. As shown in Table 3, the density correction values used in the variable density correction grid

Table 3. Lateral density correction values and terrain correction densities calculated using covariance.

Tectonostratigraphic Group	Average Density (g/cm³)	Terrain Correction Density NRV area (g/cm³)	FMB area (g/cm³)
Miramichi	2.75	2.83	*
Sheephouse Brook	2.81	*	*
Tetagouche	2.72	2.73	2.70
California Lake	2.82	2.82	2.82
Fournier	2.83	*	*
Kingsclear	2.75	*	*
Chaleurs	2.73	*	*
Dalhousie	2.72	*	*
Carboniferous sedimentary rock	2.73	*	*
Intrusives	2.75	2.40	*

* Group not present in test area

are very close to the "optimum" correction density values derived from the best-fit slope computation; however, rather than cross-referencing several grids (as in the case of the incremental terrain correction) all the information is presented in a single image (Fig. 4e). It is important to note that this method performs better in areas of rugged relief with uniform density, and it is much more difficult to apply in regions of extreme relief with multiple formations of different densities.

Magnetic Susceptibility Constraint for Frequency Domain Electromagnetic Data Inversion

Measured in-situ, magnetic susceptibly (MS_m) values were used to verify magnetic susceptibility values calculated through inversion of frequency domain electromagnetic (FDEM) data (MS_i) for a small test area north of the Tetagouche Anitform's hinge line (area bounded by rectangle shown in Figs. 1, 5a). These MS_i values are then used to forward model the local near-surface anomalous magnetic field to produce an optimal near-surface residual (Tschirhart et al., 2013). Magnetic susceptibility is recorded as a negative in-phase component by FDEM systems. Although the susceptibility signal is independent of frequency, it is most easily detected with low-frequency EM signals because at these wavelengths, conductivity, which is frequency dependent, is less dominant (Fraser, 1981; Hodges, 2004; Fig. 5b). Apparent resistivity is solved from the coplanar in-phase frequencies using a singular value decomposition inversion developed by Huang and Fraser (2000). Results of the inversion are then compared with *in situ* magnetic susceptibility values measured on 25 samples collected within the area (Fig. 5c). At four sample locations, negative MS_i values were

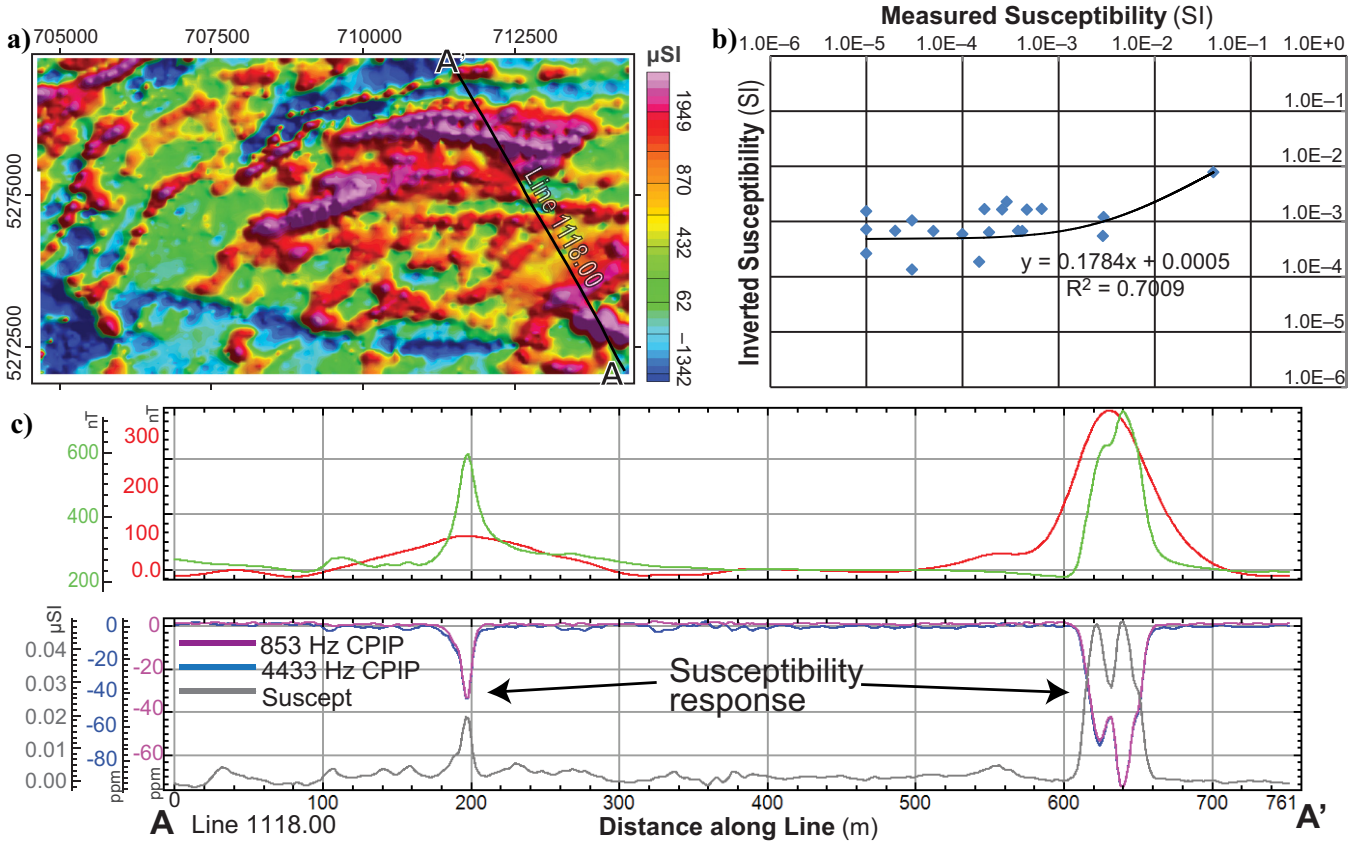

Figure 5. Apparent magnetic susceptibility inverted from frequency domain electromagnetic data: **a)** apparent magnetic susceptibility map of the test area (see Fig. 1 for location); **b)** results from Line 1118, comparing modelled and measured magnetic intensity (top) and the relationship between low- and mid-frequency coplanar in-phase response to inverted susceptibility (bottom); and **c)** bivariate plot of the inverted magnetic susceptibility value versus the measured magnetic susceptibility.

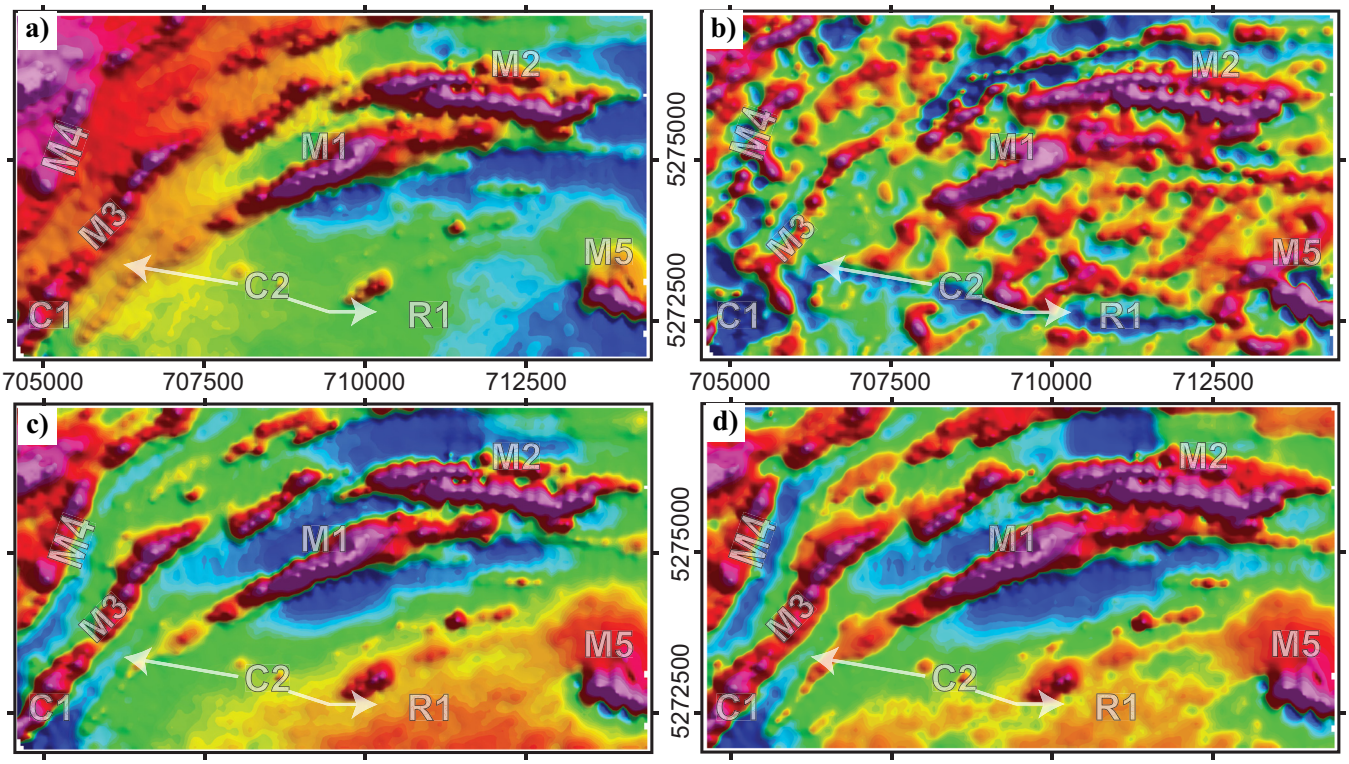

Figure 6. Plots showing the **(a)** pole-reduced total magnetic intensity map, **(b)** forward-modelled magnetic anomaly grid, **(c)** magnetic residual map constructed by removing an 800 m upward continued regional magnetic field, and **(d)** the magnetic residual map constructed by removing an 800 m non-linear filter regional magnetic field. M1 to M5 denotes prominent magnetic anomalies. R1 marks a remanent magnetic field. C1 and C2 mark conductivity anomalies.

calculated, and this arises when the EM response is dominated by surficial conductivity fluctuations. Of 21 positive MS_i values, a linear trend can be fitted between the calculated and measured magnetic susceptibilities (Fig. 5c). Discrepancies between MS_i and MS_m may be explained by the measured susceptibilities representing a single point source, whereas the inverted values represent an average of an area limited by the grid resolution, in this case: 50 x 50 m. It is also possible there may be a consistent bias in the EM signal response, producing a systematic shift in the computed susceptibility.

In order to generate an accurate near-surface magnetic anomaly map (residual) and effectively remove any deeper sourced (regional) signal, the MS_i data are forward-modelled to produce an anomalous magnetic field map (AMF_i). This map is then compared with the observed magnetic anomaly map and a suite of residual magnetic maps to select an optimal product that most closely matches the AMF_i. Figure 6 shows the total field magnetic anomaly (Fig. 6a), forward-modelled magnetic anomaly grid AMF_i (Fig. 6b), residual magnetic field that does not closely resemble the AMF_i (Fig. 6c), and a residual magnetic field that does closely resembles the AMF_i (Fig. 6d). Central to this method is that FDEM has a limited depth of penetration that is dependent upon the resistivity of the rock and frequency of the transmitting coil. Most FDEM systems have well defined effective depths of penetration, which in all cases are limited to within a couple of hundred metres below the surface. In Figure 6b, AMF_i identifies 5 prominent magnetic anomalies (annotated M1–M5) within the test area. The regional trend on this area is flat, and a proper residual must match this. Figure 6c shows a magnetic residual obtained using an 800 m upward continuation filter to model the regional field. As well, a magnetic residual produced using an 800 m non-linear filter (NLF) (Keating and Pinet, 2011) to model the regional field is shown in Figure 6d. The NLF residual generates an overall flat response, whereas the upward continuation method creates a gentle gradient in the centre of the study area (R1 area). The NLF also is superior in removing regional contributions in the northwest of the study area, which according to the AMF_i only contains thin, near-surface magnetic beds. There are some areas where the inversion poorly calculates the apparent magnetic susceptibility and subsequently incorrectly reproduces the anomalous magnetic field at these locations. Two such locations are identified in Figure 6 and labelled as C1 and C2. At location C1, there is a naturally conductive body that produces a dominant conductivity response that impedes the susceptibility response. Magnetic susceptibly is therefore not accurately recovered in the

inversion. Likewise, at location C2 a cultural source (power lines) creates a conductivity anomaly large enough to impede the susceptibility response. This therefore limits the applicability of this methodology to areas where conductivity is low. Another added benefit is that MS_i, and therefore TMI_i, are not affected by remanent magnetization and thus provide a means of mapping remanent source bodies and their relative remanent vector direction, positive or negative (Tschirhart et al., 2013).

IMPLICATIONS FOR EXPLORATION

The research reported herein has several implications for exploration. First and foremost, a comprehensive physical property database reduces the ambiguity associated with geophysical interpretation and provides ancillary information for the integration of geological and geophysical datasets. More accurate geophysical models and interpretations can therefore be developed at various scales because the physical rock property distributions are better understood. Large-scale geophysical modelling across the BMC has led to a better understanding of the deep structure of the major litho-stratigraphic units (Tschirhart and Morris, 2014). Small-scale 3-D inversions have shown the important effect of remanence within the BMC at a deposit-scale, and this method has been used to provide another independent age for mineralization in the Armstrong B deposit. This study has demonstrated that it is possible to derive regional magnetic susceptibility patterns from both aeromagnetic and frequency domain electromagnetic surveys. A pixel-by-pixel comparison of the susceptibility estimates derived from the two methods over a map area provides a method for locating regions where remanent magnetization is dominant. A density versus magnetic susceptibility bivariate plot using a Henkel (1994) template as a background serves to emphasize the presence of two geophysical manifestations of the effects of hydrothermal alteration: a) increased abundance of weakly magnetic paramagnetic minerals associated with a large density increase, and b) creation, or destruction of strongly magnetic ferrimagnetic minerals associated with a limited density increase.

Although the physical property information compiled here is specific to the BMC, the various methods developed can be applied elsewhere. Application of a variable density correction to ground and/or airborne gravity/gravity gradiometry is possible in any survey location. Similarly, the magnetic susceptibility inversion from FDEM data and its constraint to near-surface magnetic mapping is universally applicable.

ACKNOWLEDGEMENTS

The authors are grateful for the encouragement and support of Jan Peter throughout the duration of this project. Reviewers by J. Peter and V. Tschirhart greatly improved the content and clarity of this work.

REFERENCES

Currie, K.L., van Staal, C.R., Peter, J.M., and Rogers, N., 2003. Conditions of metamorphism of the main massive sulphide deposits and surrounding rocks in the Bathurst Mining Camp, *In:* Massive Sulfide Deposits of the Bathurst Mining Camp, New Brunswick, and Northern Maine, (ed.) W.D. Goodfellow, S.R. McCutcheon, and J.M. Peter; Society of Economic Geologist, Monograph 11, p. 65–78.

FitzGerald, D.J., Paterson, R., and Christensen, A.N., 2011. Decorrelating measured airborne gravity gradiometry data with topography; Geosynthesis Conference Abstract, Capetown.

Fraser, D.C., 1981. Magnetite mapping with a multi-coil airborne electromagnetic system; Geophysics, v. 46, p. 1579–1593.

Goodfellow, W.D. and McCutcheon, S.R., 2003. Geologic and genetic attributes of volcanic sediment-hosted massive sulfide deposits of the Bathurst Mining Camp, Northern New Brunswick, *In:* Massive Sulfide Deposits of the Bathurst Mining Camp, New Brunswick, and Northern Maine, (ed.) W.D. Goodfellow, S.R. McCutcheon, and J.M. Peter; Society of Economic Geologist, Monograph 11, p. 245–302.

Henkel, H., 1994. Standard diagrams of magnetic properties and density — A tool for understanding magnetic petrology; Journal of Applied Geophysics, v. 32, p. 43–53.

Hinze, W.J., 2003. Bouguer reduction density, why 2.67?; Geophysics, v. 68, p. 1559–1560.

Hodges, G., 2004. Mapping conductivity, magnetic susceptibility, and dielectric permittivity with helicopter electromagnetic data, *In:* Proceedings; Society of Exploration Geophysicists International Exposition and 74th Annual Meeting, Denver, Colorado, October 10-15, 2004, p. 660–663.

Huang, H. and Fraser, D.C., 2000. Airborne resistivity and susceptibility mapping in magnetically polarizable areas; Geophysics, v. 65, p. 502–511.

Keating, P. and Pinet, N., 2011. Use of non-linear filtering for the regional-residual separation of potential field data; Journal of Applied Geophysics, v. 73, p. 315–322.

Liss, M. J., van der Pluijm, B. A., and Van der Voo, R., 1993, Avalonian proximity of the Ordovician Miramichi Terrane, northern New Brunswick, northern Appalachians: Paleomagnetic evidence for rifting and back-arc basin formation at the southern margin of Iapetus; Tectonophysics, v. 227, p. 17–30.

Mwenifumbo, C.J., Elliot, B.E., and Street, P., 2003. Borehole geophysical characteristics of massive sulfide deposits in the Bathurst Mining Camp, *In:* Massive Sulfide Deposits of the Bathurst Mining Camp, New Brunswick, and Northern Maine, (ed.) W.D. Goodfellow, S.R. McCutcheon, and J.M. Peter; Society of Economic Geologist, Monograph 11, p. 841–860.

New Brunswick Department of Energy and Mines, 2013. New Brunswick Bedrock Lexicon, Spruce Lake Formation. http://dnr-mrn.gnb.ca/Lexicon/Lexicon/Lexicon_View.aspx. June 19, 2013

Nettleton, L.L., 1939. Determination of density for reduction of gravimeter observations; Geophysics, v. 4, p. 176–183.

Peter, J.M., Kjarsgaard, I.M., and Goodfellow, W.D., 2003. Hydrothermal sedimentary rocks of the Heath Steele Belt, Bathurst Mining Camp, New Brunswick: Part 1. Mineralogy and mineral chemistry, *In:* Massive Sulfide Deposits of the Bathurst Mining Camp, New Brunswick, and Northern Maine, (ed.) W.D. Goodfellow, S.R. McCutcheon, and J.M. Peter; Society of Economic Geologist, Monograph 11, p. 391– 416.

Rogers, N., van Staal, C.R., Winchester, J.A., and Fyffe, L.R., 2003. Provenance and chemical stratigraphy of the sedimentary rocks of the Miramichi, Tetagouche, California Lake, and Fourier Groups, Northern New Brunswick, *In:* Massive Sulfide Deposits of the Bathurst Mining Camp, New Brunswick, and Northern Maine, (ed.) W.D. Goodfellow, S.R. McCutcheon, and J.M. Peter; Society of Economic Geologist, Monograph 11, p. 111–128.

Spicer, W., 2010. Geologically Constrained Geophysical Modeling of magnetics and Gravity - the Baie Verte Peninsula, Newfoundland; M.Sc. thesis, McMaster University, Hamilton, Ontario, 166 p.

Thomas, M.D., 2003. Gravity signatures of massive sulfide deposits, Bathurst Mining Camp, New Brunswick, *In:* Massive Sulfide Deposits of the Bathurst Mining Camp, New Brunswick, and Northern Maine, (ed.) W.D. Goodfellow, S.R. McCutcheon, and J.M. Peter; Society of Economic Geologist, Monograph 11, p. 799–817.

Thomas, M.D., Walker, J.A., Keating, P., Shives, R., Kiss, F., and Goodfellow, W.D., 2000. Geophysical atlas of massive sulphide signatures, Bathurst mining camp, New Brunswick; Geological Survey of Canada, Open File 3887 (also New Brunswick Department of Natural Resources and Energy, Minerals and Energy Division, Open File 2000-4), 105 p.

Torsvik, T. H., Van der Voo, R., Preeden, U., Mac Niocaill, C., Steinberger, B., Doubrovine, P. V., van Hinsbergen, D.J.J., Domeier, M., Gaina, C., Tovher, E., Meert, J.G., McCausland, P.J., and Cocks, L.R.M., 2012. Phanerozoic polar wander, paleogeography and dynamics; Earth-Science Reviews, v. 114, p. 325–368.

Tschirhart, P.A., 2013. Geophysical processing and interpretation with geologic controls: Examples for the Bathurst Mining Camp; M.Sc. thesis, McMaster University, Hamilton, Ontario, 143 p.

Tschirhart, P.A. and Morris, W.A., 2014. Analysis of petrophysical properties of rocks from the Bathurst Mining Camp: Constraints on gravity and magnetic modelling; Interpretation, v. 2, p. SJ133–SJ150.

Tschirhart, P.A., Morris, W.A., and Hodges, G., 2013. A new regional/residual separation for magnetic data sets using susceptibility from frequency-domain electromagnetic data; Geophysics, v. 78, p. B351-B359.

Vajk, R., 1956. Bouguer corrections with varying surface density; Geophysics, v. 21, 1004–1020.

van Staal, C.R., Wilson, R.A., Rogers, N., Fyffe, L.R., Langton, J.P., McCutcheon, S.R., McNicoll, V., and Ravenhurst, C.E., 2003. Geologic and tectonic history of the Bathurst Supergroup, Bathurst Mining Camp, and its relationship to coeval rocks in Southwestern New Brunswick and adjacent Maine - A synthesis, *In:* Massive Sulfide Deposits of the Bathurst Mining Camp, New Brunswick, and Northern Maine, (ed.) W.D. Goodfellow, S.R. McCutcheon, and J.M. Peter; Society of Economic Geologist, Monograph 11, p. 37–60.

van Staal, C.R., Currie, K.L., Rowbotham, G., Goodfellow, W., and Rogers, N., 2008. Pressure-temperature paths and exhumation of Late Ordovician-Early Silurian blueschists and associated metamorphic nappes of the Salinic Brunswick subduction complex, northern Appalachians; Geological Society of America Bulletin, v. 120, p. 1455–1477.